CrossMark

Dynamical Unification of Tidal Disruption Events

Lars L. Thomsen[1] , Tom M. Kwan[1] , Lixin Dai[1] , Samantha C. Wu[2] , Nathaniel Roth[3] , and Enrico Ramirez-Ruiz[4,5]

[1] Department of Physics, University of Hong Kong, Pokfulam Road, Hong Kong, People's Republic of China; lixindai@hku.hk
[2] California Institute of Technology, Astronomy Department, Pasadena, CA 91125, USA
[3] Lawrence Livermore National Laboratory, Livermore, CA 94550, USA
[4] Department of Astronomy and Astrophysics, University of California Santa Cruz, 1156 High Street, Santa Cruz, CA 95060, USA
[5] DARK, Niels Bohr Institute, University of Copenhagen, Denmark

Abstract

The $\sim$100 tidal disruption events (TDEs) observed so far exhibit a wide range of emission properties both at peak and over their lifetimes. Some TDEs radiate predominantly at X-ray energies, while others radiate chiefly at UV and optical wavelengths. While the peak luminosities across TDEs show distinct properties, the evolutionary behavior can also vary between TDEs with similar peak emission properties. In particular, for optical TDEs, while their UV and optical emissions decline somewhat following the fallback pattern, some events can greatly rebrighten in X-rays at late time. In this Letter, we conduct three-dimensional general relativistic radiation magnetohydrodynamics simulations of TDE accretion disks at varying accretion rates in the regime of super-Eddington accretion. We make use of Monte Carlo radiative transfer simulations to calculate the reprocessed spectra at various inclinations and at different evolutionary stages. We confirm the unified model proposed by Dai et al., which predicts that the observed emission largely depends on the viewing angle of the observer with respect to the disk orientation. Furthermore, we find that disks with higher accretion rates have elevated wind and disk densities, which increases the reprocessing of the high-energy radiation and thus generally augments the optical-to-X-ray flux ratio along a particular viewing angle. This implies that at later times, as the accretion level declines, we expect that more X-rays will leak out along intermediate viewing angles. Such dynamical model for TDEs can provide a natural explanation for the diversity in the emission properties observed in TDEs at peak and along their temporal evolution.

Unified Astronomy Thesaurus concepts: Accretion (14); Astrophysical black holes (98); Black hole physics (159); Magnetohydrodynamics (1964); Radiative transfer (1335); Quasars (1319)

1. Introduction

The tidal disruption of stars by massive black holes (MBHs) offers a unique probe of MBH demographics (Mockler et al. 2019; Gezari 2021), host galaxy properties (French et al. 2020), stellar dynamics (Pfister et al. 2020; Stone et al. 2020), and black hole accretion and jet physics (Dai et al. 2021). When a star with mass $m_\star$ and radius $r_\star$ approaches an MBH with mass M_{BH}, the star is disrupted within the tidal radius $R_t \approx (M_{BH}/m_\star)^{1/3} r_\star$, where the MBH's tidal force exceeds the stellar self-gravity. About half stellar debris orbits back to the vicinity of the MBH following a characteristic pattern that first quickly increases to a peak and then declines with time following a mass fallback rate $\dot{M}_{fb} \approx t^{-5/3}$ (Rees 1988; Evans & Kochanek 1989; Guillochon & Ramirez-Ruiz 2013). When $M_{BH} \sim 10^6 M_\odot$, $\dot{M}_{fb}$ can exceed the Eddington accretion rate by two orders of magnitude at peak and stays super-Eddington for years after peak. Here we define the Eddington accretion rate of a black hole as $\dot{M}_{Edd} = L_{Edd}/(\eta_{NT} c^2)$, where $L_{edd} = 4\pi G M_{BH} c/\kappa$ is the Eddington luminosity for an opacity κ and η_{NT} is the nominal accretion efficiency for the Novikov–Thorne thin-disk solution (Novikov & Thorne 1973).

With the recent launches of all-sky transient surveys including ZTF and eROSITA, the number of detected tidal disruption event (TDE) candidates has reached around 100 (e.g., Gezari 2021; Sazonov et al. 2021; Hammerstein et al. 2022). TDEs have been categorized into two classes based on their main emission type at peak: X-ray TDEs (Auchettl et al. 2017; Saxton et al. 2021) and optical TDEs (van Velzen et al. 2020). Most X-ray-selected TDEs emit soft X-rays with effective temperatures at $10^5 - 10^6$ K, while only three of them emit beamed, hard X-rays that are associated with relativistic jets (e.g., Bloom et al. 2011; Burrows et al. 2011; Cenko et al. 2012; De Colle et al. 2012). In contrast, the optical TDEs have lower effective temperatures of a few $\times 10^4$ K. Interestingly, as the luminosity of a TDE typically declines by around one order of magnitude over tens to hundreds of days after peak, its effective temperature usually undergoes a peculiar nonevolution. Recently, a large number of TDEs have been followed up for longer than a year. Rather surprisingly, a few initially optically strong TDEs brighten in X-rays, so that their X-ray and UV/optical fluxes reach similar levels after about a year (e.g., Gezari et al. 2017; Holoien et al. 2018; Wevers et al. 2019; Hinkle et al. 2021; Liu et al. 2022).

Many theoretical models have been proposed to explain these TDE emission properties (Roth et al. 2020). While the X-ray emissions have been predicted by classical accretion disk models (Ulmer 1999), UV/optical emissions are argued to be produced from either the reprocessing of X-ray photons in an extended envelope or outflows (Loeb & Ulmer 1997; Strubbe & Quataert 2009; Lodato & Rossi 2011; Coughlin & Begelman 2014; Guillochon et al. 2014; Metzger & Stone 2016; Roth et al. 2016; Parkinson et al. 2020, 2022) or the shocks powered by debris stream self-intersection (Piran et al. 2015;

Bonnerot et al. 2021). The late-time rebrightening of X-rays in TDEs can be accounted for by either a change in the disk morphology as the accretion rate declines from super-Eddington to sub-Eddington or the delayed onset of accretion (van Velzen et al. 2019; Hayasaki & Jonker 2021). The latter model, however, is disfavored by recent simulations showing that a large fraction of the debris already settles into a disk with moderate eccentricity within dynamical times for at least a subset of TDE parameters (Bonnerot et al. 2021; Andalman et al. 2022).

In search for a unified model that can explain both the optical and X-ray TDEs, Dai et al. (2018) have carried out the first three-dimensional (3D) general relativistic radiation magneto-hydrodynamics (GRRMHD) simulation tailored for TDE super-Eddington accretion flow. The simulated disk, around a black hole with $M_{BH} = 5 \times 10^6 \, M_\odot$ and spin parameter $a = 0.8$, has an accretion rate of $\dot{M}_{acc} \sim 10 \, \dot{M}_{Edd}$, representing a typical accretion level in TDEs. The spectra of the disk have been obtained by post-processing the simulated disk with a novel radiative transfer code. It is found that the observed emission type largely depends on the viewing angle of the observer with respect to the disk orientation. When viewed face-on, X-ray emissions can escape from the optically thin funnel surrounded by winds. When viewed edge-on, X-ray emissions are heavily reprocessed in the geometrically and optically thick wind and disk, so only UV/optical emissions can be observed.

While this study gives a good first-order description of TDE disks and spectra, recent simulations also show that the properties of a super-Eddington disk depend on the accretion rate, the black hole mass and spin, and the magnetic flux threading the disk (Jiang et al. 2014; McKinney et al. 2015; Sądowski & Narayan 2016; Jiang et al. 2019). Although the black hole spin and disk magnetic flux might only mildly affect the main structure of the disk, they determine whether a relativistic jet can be launched (Blandford & Znajek 1977; Curd & Narayan 2019). At first glance, the black hole mass is not expected to affect the disk spectra significantly, since most TDE host MBHs have masses in a narrow range $\approx 10^5$–$10^7 \, M_\odot$. However, the peak fallback rate of the TDE debris sensitively depends on the black hole mass with the relation $\dot{M}_{fb,peak}/\dot{M}_{Edd} \propto M_{BH}^{-3/2}$. Therefore, TDEs from smaller MBHs should in general have much higher accretion rates at peak than those from larger MBHs (Ramirez-Ruiz & Rosswog 2009). In addition, further variance of the accretion rates in different TDEs as $\dot{M}_{fb,peak}$ can be introduced by the difference in the masses and ages of the disrupted stars (Law-Smith et al. 2020).

In this Letter, we investigate how the TDE disk structure and the accompanied emission are influenced by the accretion rate at super-Eddington rates. We conduct three 3D GRRMHD simulations of super-Eddington disks with similar structures but varying accretion rates and post-process the simulated disks to obtain their spectra at different inclination angles. These simulations are useful for understanding the diversity of the emissions observed from different TDEs, as well as the evolution of single TDEs as their fallback and accretion rates decline after peak. In Section 2 we introduce the setup of the GRRMHD and radiative transfer simulations. In Section 3 we give the main results and compare with TDE key observables. In Section 4 we draw a summary and discuss the implications and future work.

Table 1
Black Hole and Accretion Disk Parameters

Model	M_{BH} ($M_\odot$)	a	$\dot{M}_{acc}$ ($\dot{M}_{Edd}$)	$\dot{M}_w$ ($\dot{M}_{Edd}$)	L_{RAD} (L_{Edd})
M6a08-1	10^6	0.8	7	1.4	5.4
M6a08-2	10^6	0.8	12	4.5	3.3
M6a08-3	10^6	0.8	24	14	8.1

2. Methodology

2.1. Disk Simulation Setup

We carry out 3D simulations of super-Eddington disks using a fully GRRMHD code HARMRAD with M1 closure (McKinney et al. 2014). In all simulations the MBH has $M_{BH} = 10^6 \, M_\odot$ and $a = 0.8$. The radial grid has 128 cells spanning from $R_{in} \approx 1.2 R_g$ to $R_{out} = 8500 R_g$ ($R_g = GM_{BH}/c^2$ is the gravitational radius of the MBH), with cell size increasing exponentially until $R_{break} \approx 500 R_g$ and then increasing hyper-exponentially. The θ-grid has 64 cells spanning from 0 to π with finer resolution in the jet and disk regions. The ϕ-grid has 32 grids spanning uniformly from 0 to 2π with periodic boundary conditions. The gas is assumed to have solar chemical abundances (mass fractions of H, He, and "metals," respectively, $X = 0.7$, $Y = 0.28$, $Z = 0.02$). Frequency-mean absorption and emission opacities are used as in McKinney et al. (2015), except that the Chianti opacity is removed, as it is unimportant for the disk temperature of our TDE models. Thermal Comptonization is also included.

We tailor the disk initial conditions to be consistent with realistic TDE scenarios following the setup described in Dai et al. (2018). The accretion disk is initialized with Keplerian velocity profile with a rest-mass density that is Gaussian in angle with a height-to-radius ratio of $H/R \approx 0.3$, so that the initial density profile is given by

$$\rho(r, z) = \rho_0 r^{-1.3} e^{-z^2/(2H^2)}, \tag{1}$$

where H is the scale height and ρ_0 is the initial reference density. The initial disks in the three simulations have masses varying in the range of a few $\times$ (0.1–1) $M_\odot$. Adjusting ρ_0 leads to different accretion rates after the disk reaches the quasi-equilibrium state. As $\dot{M}_{fb,peak}$ can reach $\approx 100 \dot{M}_{Edd}$ in a TDE around a $10^6 \, M_\odot$ black hole, and a large fraction of the debris mass is expected to escape in outflows, we set the aimed accretion rates to be a few to a few tens of $\dot{M}_{Edd}$ (Table 1).

A large-scale poloidal magnetic field is initially seeded. As adopted in McKinney et al. (2015), for r smaller than a breaking radius $R_b = 500 R_g$, the ϕ component of the vector potential is given by $A_\phi = \text{MAX}(r \, 10^{40} - 0.02, 0)(\sin \theta)^5$. For $r \geqslant R_b$, the field transitions to a split monopolar field, which is given by $A_\phi = \text{MAX}(R_b \, 10^{40} - 0.02, 0)(\sin \theta)^{1+4(R_b/r)}$. The field is normalized so that the initial ratio of gas+radiation pressure to magnetic pressure $\beta \equiv (p_{gas} + p_{rad})/p_b$ has a minimum value of 10.

2.2. Radiative Transfer Setup

We use the Monte Carlo radiative transfer code Sedona (Kasen et al. 2006) to post-process the simulated disks and calculate the escaping radiation. More specifically, we calculate the bound electron level populations under non-local thermal equilibrium as in Roth et al. (2016) and the Comptonization of

electrons as in Roth & Kasen (2018). We track the free–free interactions, as well as the bound–bound and bound–free interactions. The bound–bound cross sections are obtained from the atomic database CMFGEN, and the bound–free cross sections are calculated using the hydrogenic approximation

$$\sigma_{bf}(\nu, n_{pq}, Z) = \begin{cases} \sigma_0 n_{pq}/Z^2 \ (\nu/\nu_{tresh})^{-3}, & \text{if } \nu > \nu_{thresh}. \\ 0, & \text{otherwise.} \end{cases} \quad (2)$$

Here $\sigma_0 = 6.3 \times 10^{-18} \text{cm}^2$, n_{pq} is the principal quantum number, Z is the nuclear charge of the ion, ν is the photon frequency, and ν_{tresh} is the ionization threshold frequency set by the binding energy of the (least) bound electron. The gas is assumed to consist of only H, He, and O with solar abundances. For the radiative transfer calculations in this work, we focus on calculating the spectral energy distribution (SED) and leave the line modeling to a future study that requires higher-frequency resolution to accurately resolve the intrinsic narrow line width.

For each accretion rate, we calculate the spectra for four inclination bins at $\theta_{bin} = 10°$, $30°$, $50°$, and $70°$. In each bin, we take an average over $\theta_{bin} \pm 5°$ for the already time-ϕ-averaged profile of the simulated disk. Since the simulated jet density is likely numerically boosted, for the bins at $\theta_{bin} = 10°$ and $30°$ we also reduce the jet density by 100 times before taking the average. We note that the first-order behavior of the spectra does not depend on this arbitrary choice of density rescaling inside the jet. We set the source to be a blackbody spectrum with a single temperature of 10^6 K, which is consistent with the inner disk temperature. The source photons are injected from an inner boundary set at the boundary between the inflow and outflow, which is typically at a few R_g except for the bin at $\theta_{bin} = 70°$, which is partly in the disk inflow region. For the latter, we place the inner boundary at $R = 20R_g$ instead and set the gas velocity to be always zero. The photons are then propagated in 3D, by assuming that the gas density, temperature, and radial velocity profiles are spherically symmetric. The photons propagate outward until they leave the computational domain set at $R = 4000R_g$ or have become a part of the kinetic/thermal pool. The total masses of the accretion flow in the regions we have used for post-processing ($i = 0°$–$75°$) are 0.012, 0.024, and 0.072 $M_\odot$ for the three simulations.

Based on the Monte Carlo calculations, we iterate the gas temperatures, gas ionization state, bound electron states, and radiative transfer solution under the assumption of radiative equilibrium until a steady solution has been reached (after approximately 20 iterations). Since GRRMHD simulations show that the luminosities of super-Eddington disks are not always capped by L_{Edd}, we also tweak the source photon luminosity and obtain the spectra under two limits—the escaped bolometric luminosity is either $L_{bol} = L_{Edd} \approx 10^{44}$ erg s^{-1} or $L_{bol} = 0.1 \, \dot{M}_{acc}c^2 \approx (\dot{M}_{acc}/\dot{M}_{Edd}) \, L_{Edd}$.

3. Results

3.1. Properties of the Accretion Flow

In all three GRRMHD simulations, it takes an initial time period of $t = \text{few} \times 1000R_g/c$ for the accretion flow to get established. As the disk evolves, magnetic fluxes accumulate near the MBH and their strength further grows via the magnetorotational instability (MRI; Balbus & Hawley 1998). Here we focus on the final stage of the simulations when the

accretion flow has reached steady state and the wind has established equilibrium at most inclination angles. The black hole parameters and some basic quantities of the accretion disks, averaged over the period of $t = (15,000 - 20,000) \, R_g/c$, are listed in Table 1. The disk profiles used for post-processing are also first ϕ-averaged and then time-averaged over the same period. More numerical details of the simulated disks are given in Appendix A.

The averaged accretion rates onto the event horizon of the MBH in these three simulations are $\dot{M}_{acc} \approx (7, 12, 24)\dot{M}_{Edd}$. To first order, these super-Eddington accretion flows have similar structures to those described in Dai et al. (2018). As shown in the top panels of Figure 1, geometrically and optically thick disks are formed with half-angular thickness $H/R \approx 0.20$–0.25, with, as expected, higher gas density toward the equatorial plane. The disks have achieved quasi-equilibrium for the inner $200R_g$–$300R_g$ region. The rotation profile of the resultant thick disks is sub-Keplerian. Wide-angle winds are launched by the large radiation and magnetic pressure, which are also optically thick at most angles except close to the polar axis. There are roughly two components of the wind: an ultrafast outflow (UFO) with speeds faster than $0.1c$ within $\lesssim 45°$ from the pole, and a slower but denser wind outside $\gtrsim 45°$ inclination. At larger accretion rates, the disk and wind densities increase, and the winds become slower as a result of mass loading. However, the wind geometry stays fairly similar.

The emission properties of the accretion flow should be examined near the photosphere. The optical depth for an opacity κ is calculated using $\tau(r) = \int \rho \kappa dl$ along the radial direction, r, from the outer boundary $R_{out} = 8500R_g$ toward the event horizon. (Here relativistic effects are included so that $dl = -f_\gamma dr$, with $f_\gamma \approx u^t(1 - v/c)$ and $v/c \approx 1 - 1/(u^t)^2$.) The electron-scattering photosphere is defined by $\tau_{es}(r) = 1$ with $\kappa = \kappa_{es} \approx 0.2(1 + X)$ cm^2 g^{-1}. The effective photosphere is then defined by $\tau_{eff}(r) = 1$ with $\kappa = \kappa_{eff} = \sqrt{3\kappa_{ff}(\kappa_{ff} + \kappa_{es})}$, where we have only considered free–free opacity $\kappa_{ff} \approx 3.82 \times 10^{22}Z(1 + X)(1 - Z)\rho T_g^{-3.5}$ in the scattering-dominated gas, where T_g is the gas temperature. Both photospheres are plotted over the disk profiles in the bottom panels of Figure 1. As expected, we see the presence of an optically thin "funnel" near the rotation axis where the wind density is correspondingly lower. As the accretion rate increases, the wind becomes more opaque, which reduces the angular size of the funnel.

The effective photospheres reside mostly within $r \sim 5000R_g$ except along the equatorial direction for the disk with the largest $\dot{M}_{acc}$. Therefore, we select to evaluate various physical quantities at $r = 5500R_g$. This gives averaged wind mass rates of $\dot{M}_w = (1.4, 4.5, 14)\dot{M}_{Edd}$ and averaged bolometric luminosities at $L_{RAD} = (5.4, 3.3, 8.1)L_{Edd}$, respectively, for the three simulations. The radiation temperature of the accretion flow is also plotted, which varies from $\approx 10^6$ K near the black hole to $\approx 10^4$ K in the outer part of the disk and wind. The radiation flux varies with the inclination as shown in Dai et al. (2018) and leaks out through the region of least resistance, which is the funnel.

Magnetic fluxes are dragged by the accretion flow and accumulate near the MBH. The inner disk regions quickly enter the regime of magnetically arrested accretion disks (MADs; Narayan et al. 2003). Relativistic jets are launched magnetically through the Blandford–Znajek mechanism (Blandford & Znajek 1977) in all simulations. In this Letter we focus on
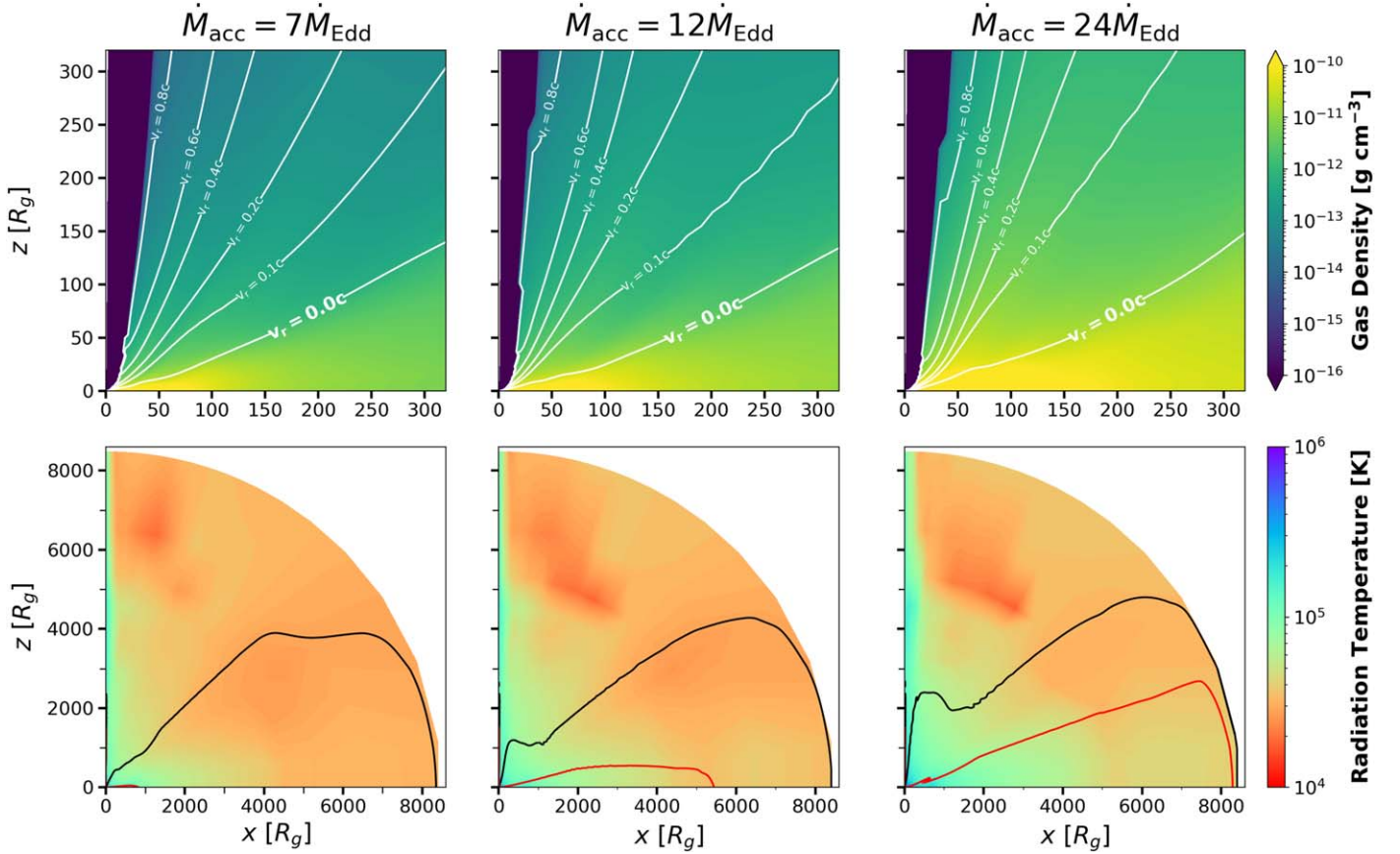
Figure 1. The 2D vertical profiles of time-ϕ-averaged gas rest-mass density ρ_0 (top panels, zoomed into the inner regions) and radiation temperature $T_{\rm RAD}$ (bottom panels, whole range of the simulation box), for the three runs with different accretion rates (from left to right: $\dot{M}_{\rm acc} = 7\dot{M}_{\rm Edd}$, $12\dot{M}_{\rm Edd}$, and $24\dot{M}_{\rm Edd}$) in the quasi-equilibrium state. In the top panels, we show the contours of constant lab-frame radial velocity ($v_r \equiv u^r/u^t$) with white lines and show the jet regions, where the electromagnetic energy is larger than the rest-mass energy of the gas, in dark blue. In the bottom panels, the black lines indicate the electron-scattering photosphere with $\tau_{\rm es} = 1$, and the red lines indicate the effective photosphere with $\tau_{\rm eff} = 1$. Larger accretion rates induce larger disk/wind density and higher gas/radiation temperature, while the gas distribution and velocity structure remain rather robust against the variance in accretion rates. The sizes of photospheres generally increase as accretion rate increases.

calculating the emission properties from the disk, and we leave the analysis of the jets for future study.

3.2. Spectra from Post-processing

In this section we investigate how the emission reprocessing depends on a few key parameters, namely, the viewing angle, the accretion rate, and the luminosity. The dependence on viewing angle has been previously studied by Dai et al. (2018). They show that for a fixed accretion rate there is a clear trend of the SED moving toward larger wavelengths with increasing inclination angle. At low inclinations, the gas density is lower, so X-rays produced from the inner disk easily escape. At relatively large inclinations, on the other hand, the optically thick wind and outer disk serve as an effective reprocessing envelope. More specifically, in the fast wind region, the photons lose energy as they go through multiple scatterings in the expanding outflow before escaping. In the disk and the slow wind region, the reprocessing is mainly caused by the absorption of X-ray photons and the thermal Comptonization of electrons.

We reexamine the emission viewing angle dependence in the three new simulated disks. Figures 2(a), (b), and (c) show how the escaped spectrum varies with inclination, when $\dot{M}_{\rm acc} = (7, 12, 24)\dot{M}_{\rm Edd}$, respectively. The escaped spectra are calculated from the inclination bins at $i = 10°$, $30°$, $50°$, and $70°$, with the first three bins residing in the wind and the last one

at the boundary between the wind and disk. The properties of gas in these bins are mostly set by the winds launched from the inner disk that has achieved quasi-equilibrium state and has specific angular momentum smaller than that of the disrupted star. At any of these accretion rates, the SED still evolves from X-ray to optically dominated as the inclination increases. However, the exact angle at which this transition occurs depends on the accretion rate. One can clearly observe that at low accretion rates $\approx$few $\times\ \dot{M}_{\rm Edd}$ the escaped emission is dominated by X-ray emission at most inclinations unless the inclination angle is substantial (e.g., $i \gtrsim 70°$ for $\dot{M}_{\rm acc} = 7\ \dot{M}_{\rm Edd}$), while at very high accretion rates $\approx$few $\times\ 10\ \dot{M}_{\rm Edd}$ the emanating radiation is mainly optically dominated except near the polar region (e.g., $i \lesssim 10°$ for $\dot{M}_{\rm acc} = 24\ \dot{M}_{\rm Edd}$). For a more detailed discussion of the radiative transfer physics, see Appendix B.

We expect a TDE to be observed along a fixed viewing angle during its entire evolution, unless the disk experiences some axial precession. Therefore, we show the spectral evolution with $\dot{M}_{\rm acc}$ at fixed inclination angles in Figures 2(e)–(h). As the accretion rate declines after peak, the amount of reprocessing material is reduced, so the SED universally shifts toward lower wavelengths. However, the exact behavior of the spectrum depends sensitively on the inclination angle. At very small inclinations $(i = 10°)$, the TDE stays X-ray dominated throughout its evolution. At intermediate inclinations $(i = 30°$ and $50°)$, the TDE can be optically strong at early times (if $\dot{M}_{\rm acc}$
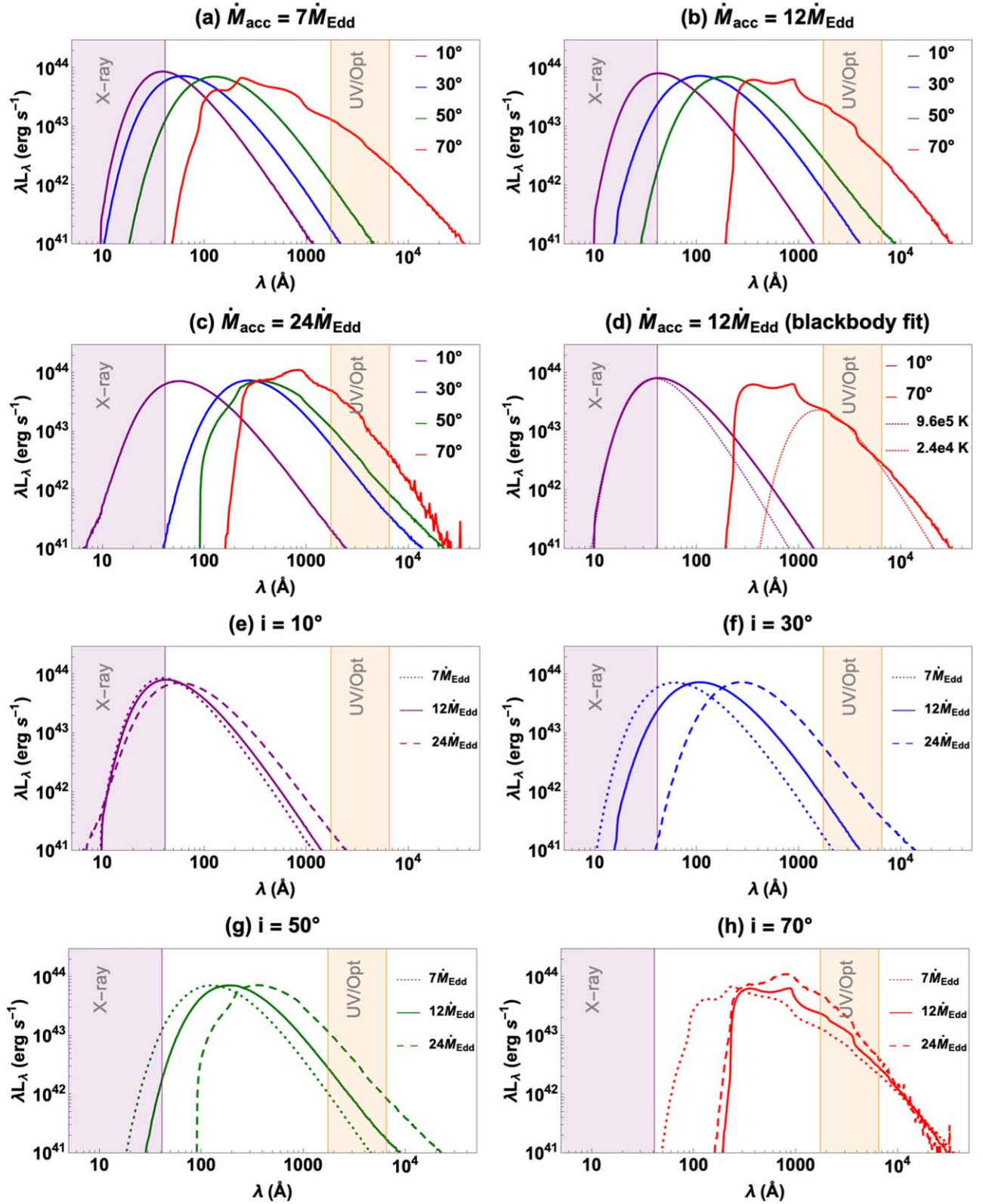
Figure 2. The simulated escaping spectra of the accretion disk at different accretion rates ($\dot{M}_{acc} = (7, 12, 24)\dot{M}_{Edd}$) and inclinations ($i = 10°, 30°, 50°, 70°$). The bolometric luminosity of the spectra $L_{bol} = L_{Edd}$ for all spectra. The purple shaded region indicates the X-ray band with an energy above 0.3 keV. The orange shaded region corresponds to Swift UVOT band at 1700–6500 Å. Panels (a)–(c) show the spectral evolution with inclination angles at fixed accretion rate. All spectra change from X-ray strong to UV/optical strong as the inclination goes from the polar direction to the disk direction. Panel (d) is the same as panel (b) but only includes the spectrum at $i = 10°$ with a blackbody spectrum fitting its X-ray continuum component and the spectrum at 70° with another blackbody spectrum fitting its UV/optical continuum component. Panels (e)–(h) show the spectral evolution with accretion rates at fixed inclinations. Three types of evolution can happen as accretion rate decreases: X-ray strong all the time (small inclination), optical/UV strong at early time and X-ray rebrightening at late time (intermediate inclination), and optical/UV strong all the time (large inclination).

can be sufficiently large) and then rebrightens at X-ray energies at late time when the accretion rate diminishes. At very large inclinations ($i = 70°$), the TDE stays UV/optically strong throughout its entire evolution.

While we have assumed that the bolometric luminosities of the escaped radiation are always close to L_{Edd} in the analysis above, GRRMHD simulations show that the true escaped luminosity from super-Eddington disks can exceed the Eddington limit, with more flux leaking out through the funnel (e.g., Sądowski & Narayan 2016). Therefore, we also calculated the spectra when the escaped radiation has a bolometric luminosity $L_{bol} = 10\% \, \dot{M}_{acc} c^2$, which are shown in Figure C1. When the reprocessing is driven by adiabatic expansion, the SED shape stays unchanged while the magnitude of the flux scales with the luminosity. When reprocessing mechanism is driven by absorption and Comptonization, increasing the luminosity makes the gas more ionized and reduces bound–free and free–free absorption, which shifts the spectral energy peak to slightly higher energies. However, the spectral shape is rather insensitive to the luminosity. In general, the setting of the luminosity within the explored range does not alter how the escaped radiation depends on the viewing angle and accretion rate.

3.3. Comparison with Observations: Blackbody Luminosity, Temperature, and Photosphere Radius

In this section, we compare our model predictions to the observed properties of TDEs. We start from the TDE catalog in Gezari (2021), which also lists the observed blackbody luminosities and temperatures, and then only include TDEs that have their masses estimated from the M–σ relation as in Wong et al. (2022). This gives us 7 X-ray selected TDEs (Table D1) and 16 optically selected TDEs (Table D2). We plot their observed blackbody luminosities, temperatures, and photosphere radii as functions of M_{BH} in Figures 3(a)–(c). The observed L_{BB} varies between $10^{-3} L_{Edd}$ and $10 L_{Edd}$ and can exceed L_{Edd} when $M_{BH} \lesssim 10^6 \, M_\odot$. Interestingly, L_{BB} commonly has a dependence on M_{BH} following the fallback rate trend: $\dot{M}_{fb}/\dot{M}_{Edd} \propto M_{BH}^{-3/2}$. The observed T_{BB} clearly depends on whether the TDE is optically selected ($\approx$few $\times 10^4$ K) or X-ray selected ($\approx 10^5$–10^6 K). The observed R_{BB}, calculated from L_{BB} and T_{BB} using the Stefan–Boltzmann law, also has a bimodal distribution. The optically selected TDEs have R_{BB} reaching $10^2 - 10^4 R_g$ and always exceeding both the circularization radius $R_{circ} = 2R_t$ and the stream self-intersection radius R_{int} (Dai et al. 2015). The X-ray-selected TDEs, however, sometimes have R_{BB} even within the event horizon. This puzzling issue has also been noted by Yao et al. (2022), who propose a few possible causes, including (1) the measured temperature being higher than the true temperature owing to Comptonization effects, and (2) the existence of some patch obscuring material that suppresses the X-ray flux without changing its spectral shape, though the nature of the material is uncertain. We point out that the large uncertainty in TDE host black hole mass estimates might also contribute to this issue.

As the observed properties of TDEs are usually inferred from their spectra in monochromatic bands, we also fit the simulated spectra in either the X-ray or UV/optical band with blackbody spectra. For example, in Figure 2(d) we show the simulated escaped spectra for $\dot{M}_{acc} = 12\dot{M}_{Edd}$ at $i = 10°$ and $70°$ and the blackbody radiation fits to the spectra in the X-ray band (0.3–10 keV) or the part of the spectrum in the UV/optical

band (the 170–650 nm Swift UVOT band). It can be seen that the X-ray and UV/optical emission can be individually well approximated by blackbody radiation. Similarly, for each spectrum (at $\dot{M}_{acc}=$ (7, 12, 24)$\dot{M}_{Edd}$ and inclination $i = 10°$, 30°, 50°, 70°), we obtain two blackbody radiation fits in the X-ray band and the UV/optical band. The escaped bolometric luminosity is assumed to be varying between L_{Edd} and $0.1\% \, \dot{M}_{acc} c^2$. The luminosities, temperatures, and radii of the best-fit blackbody radiation spectra are listed in Table E1 and plotted in Figures 3(d)–(f) (UV/optical fit) and Figures 3(g)–(i) (X-ray fit). We further categorize whether a modeled TDE spectrum is X-ray strong or optically strong by comparing the luminosity in the X-ray band (0.3–10 keV) and the blackbody luminosity inferred from the UV/optical band. We compare the model predictions to the observed properties as below:

1. *Luminosity*: The modeled L_{BB} mostly lies between $0.01 L_{Edd}$ and a few L_{Edd}. The simulated spectrum usually peaks in EUV and has a broader shape than a single-temperature blackbody spectrum. Therefore, the inferred blackbody luminosity ($L_{O,BB}$ or $L_{X,BB}$) is always smaller than the bolometric luminosity L_{bol} of the escaped radiation. $L_{O,BB}/L_{bol}$ for optically strong TDEs and $L_{X,BB}/L_{bol}$ for X-ray-strong TDEs are typically a few $\times$ (1%–10%) (Figure E1). This naturally explains the missing energy problem in TDE (Stone & Metzger 2016; Lu & Kumar 2018; Mockler & Ramirez-Ruiz 2021)—the majority of the energy is emitted in the EUV band, which is difficult to detect.

2. *Temperature*: Our modeling reproduces the bimodal distribution of TDE temperatures, i.e., optically strong TDEs have temperature $T_{O,BB} \approx$ few $\times 10^4$ K, and X-ray-strong TDEs have temperature $T_{X,BB} \lesssim 10^6$ K. Furthermore, our modeling shows that the inferred temperatures of optical TDEs are not highly sensitive to accretion rates or observer inclination, which explains why TDEs have relatively constant T_{BB} throughout the evolution (van Velzen et al. 2020).

3. *Photosphere radius*: The optically strong TDEs have far larger photosphere radii ($R_{O,BB} \approx 10^2 R_g - 10^4 R_g$) than X-ray-strong TDEs ($R_{X,BB} \approx$ few $\times R_g$). A comparison between the observed $R_{O,BB} = 10^3 R_g - 10^4 R_g$ and the modeled $R_{O,BB}$ suggests that optically selected TDEs either are commonly observed from large inclinations or have $L_{bol} > L_{Edd}$.

We note that our predictions for the X-ray quantities, particularly in the $i = 10°$ bin, are sensitive to the setting of the radiative transfer calculations. Here we always inject a blackbody spectrum with a constant $T = 10^6$ K, so our predicted $T_{X,BB}$ at small inclinations also fall into a very narrow range. However, the temperatures at the center of accretion disks generally increase with increasing $\dot{M}_{acc}$ and decreasing M_{BH}, which will induce more variance to the observed X-ray temperatures. In addition, for the setting with $L = L_{Edd}$, the predicted $L_{X,BB}$ decreases as $\dot{M}_{acc}$ increases, as a result of a constant bolometric luminosity and more reprocessing from X-ray to UV/optical emissions at higher densities. However, simulations show that the radiation fluxes leaking out through the funnel are not Eddington limited (McKinney et al. 2015; Dai et al. 2018). Therefore, we expect that X-ray luminosities should scale positively with accretion rates, as illustrated by the $L = 0.1 \, \dot{M}_{acc} c^2$ case.
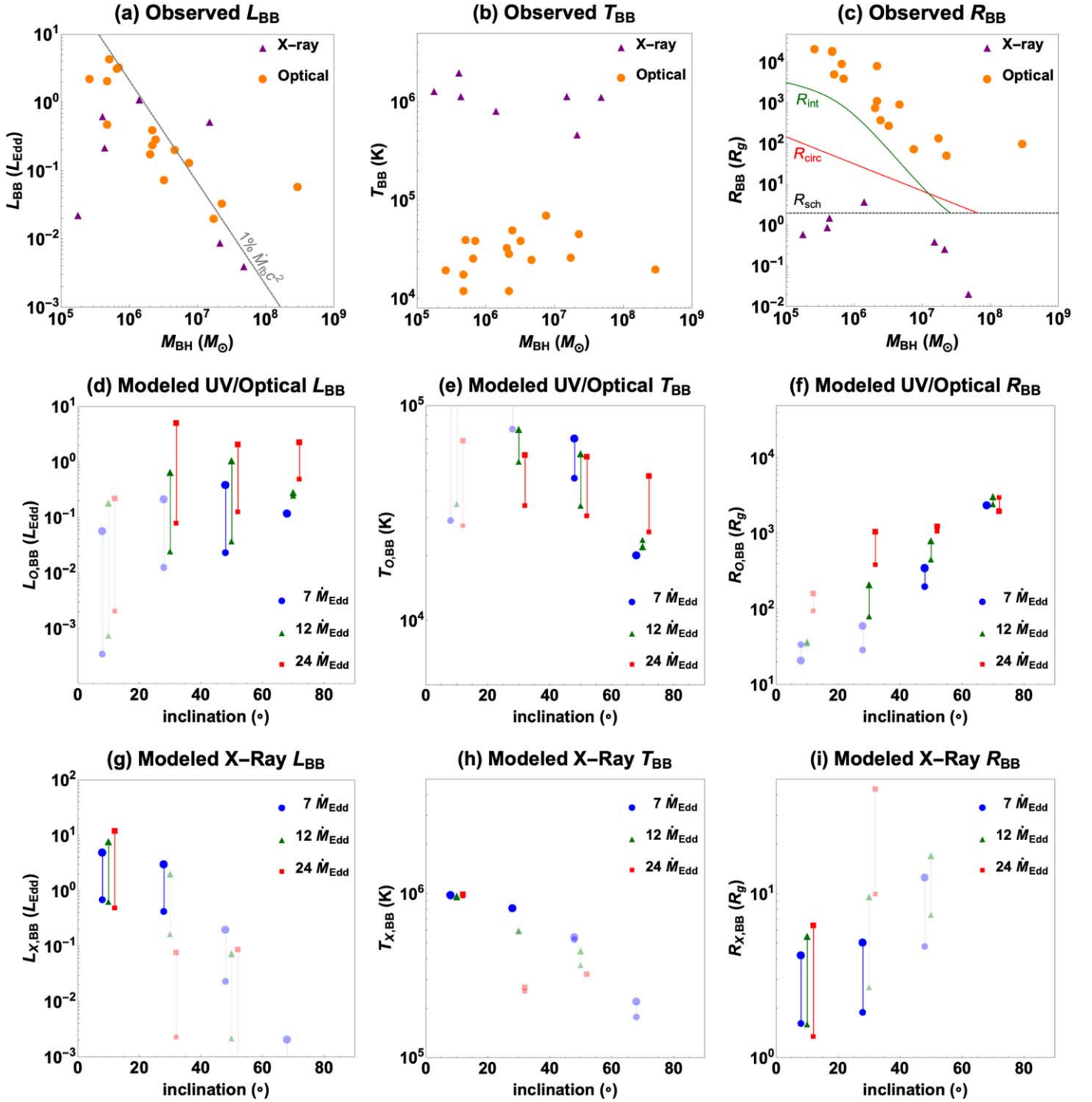
Figure 3. Comparison between the observed and modeled TDE blackbody luminosity, temperature, and radius. Top row (a–c): The observed quantities versus M_{BH} for 16 optically selected TDEs (orange circles) and 7 X-ray-selected TDEs (purple triangles). (a) The observed L_{BB}/L_{Edd} has a clear trend with M_{BH}. A gray line showing $L = 1\% \dot{M}_{fb}c^2$, with $\dot{M}_{fb}$ being the fallback rate of a 0.1 $M_\odot$ star, is overplotted to guide the eye. (b) X-ray TDEs have temperatures of $10^5 - 10^6$ K, and optical TDEs typically have lower temperatures of a few $\times 10^4$ K. (c) Optical TDEs have R_{BB} larger than the circularization radius (red curve) or the stream self-intersection radius (green curve) (both calculated using a 0.1 $M_\odot$ star). X-ray TDEs can sometimes have R_{BB} smaller than the black hole Schwarzschild radius (black line). Middle row and bottom row (d–f, g–i): The inferred quantities based on the blackbody radiation spectrum fitting the simulated spectra in the UV/optical band and X-ray band, respectively, vs. inclination angle i. Different symbols are used to mark different accretion rates: $7\dot{M}_{Edd}$ (blue circle), $12\dot{M}_{Edd}$ (green triangle), and $24\dot{M}_{Edd}$ (red square). Vertical lines connect the values calculated with an escaped luminosity of $L_{bol} = L_{Edd}$ (smaller symbol size) and $L_{bol} = 10\%\dot{M}_{acc}c^2$ (larger symbol size) to indicate possible ranges. In panels (d)–(f), TDEs with $L_{O,BB} < L_{X,0.3-10\,keV}$ are marked with lighter shaded symbols to indicate that they are less likely to be selected optically. Similarly, in panels (g)–(i), TDEs with $L_{O,BB} > L_{X,0.3-10\,keV}$ are marked with lighter shaded symbols to indicate that they are less likely to be selected by X-ray instruments. The blackbody luminosity, temperature, and radius inferred from our modeling, to the first order, reproduce the observed ones.
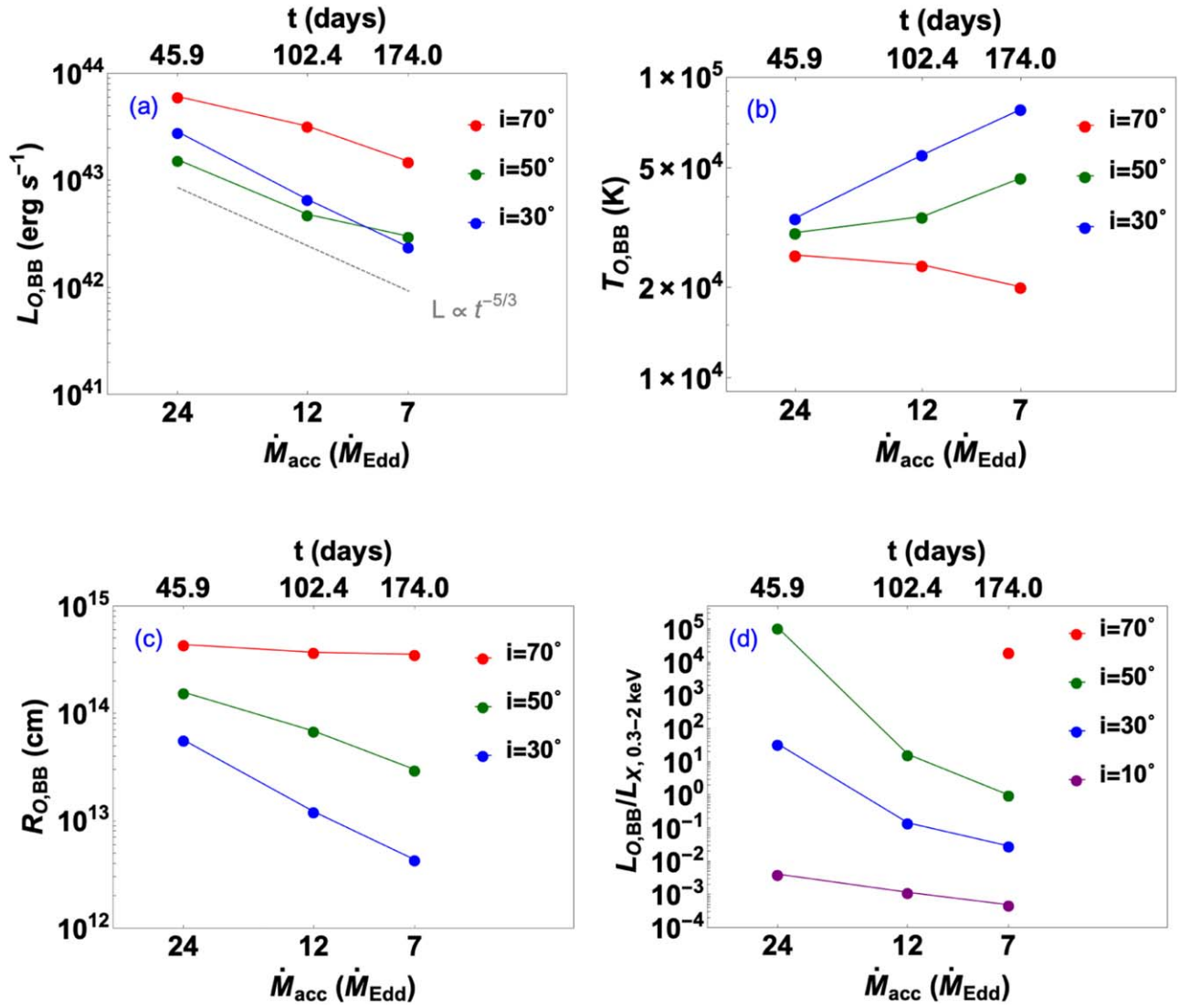
Figure 4. The post-peak temporal evolution of (a) the modeled TDE UV/optical luminosity, (b) temperature, (c) radius, and (d) the ratio between the UV/optical and X-ray luminosity. Different colors denote different inclination angles. The escaped radiation has luminosity $L_{bol} = L_{Edd}$ for all curves. The lower axis shows the accretion rate, and the upper axis shows the corresponding time elapsed since the peak, assuming a solar-type star disrupted by a $10^6 M_\odot$ black hole. In panels (a)–(c), we do not include the evolution $i = 10°$, where the event is always X-ray strong. In panel (a) the gray line shows the trend of $t^{-5/3}$ to guide the eye. In panel (d) the X-ray luminosity includes only the flux in the 0.3–2 keV band for direct comparison with observations. In addition, at $i = 70°$ the X-ray luminosities at the two higher accretion rates are negligible.

3.4. Temporal Evolution of TDE Continuum Emissions

We show in Figure 4 the evolution of the modeled luminosity, temperature, radius, and the ratio of optical to X-ray luminosity, as functions of the accretion rate. In order to connect the snapshots at a specific accretion rate to the temporal evolution of TDEs, we assume $\dot{M}_{fb}(t) = \dot{M}_{acc}(t) + \dot{M}_{wind}(t)$. This assumption is valid only if the fallback timescale dominates over other timescales, such as the disk viscous timescale and the photon diffusion/advection timescales. The exact conversion from $\dot{M}_{fb}$ to t depends on the mass of the MBH, the properties of the disrupted star, and the impact parameter (Law-Smith et al. 2020). Focusing on the post-peak evolution, the three disk simulations correspond to 45.9, 102.4, and 174 days after the peak of the flare, assuming that a solar-type star is fully disrupted by a $10^6 M_\odot$ black hole. Calculations of these timescales are given in Appendix F to show that the fallback timescale dominates over the photon transport and disk viscous timescales.

As the accretion rate drops from $24\dot{M}_{Edd}$ to $7\dot{M}_{Edd}$, the optical luminosity also decreases, and the UV/optical light curve roughly follows the canonical $t^{-5/3}$ decay. As discussed in the previous section, the fitted blackbody temperature stays rather constant. Interestingly, at large inclinations $T_{O,BB}$ slightly decreases with declining $\dot{M}_{acc}$, while at small to intermediate inclinations $T_{O,BB}$ shows the opposite trend. This can provide an explanation to the different observed evolution of $T_{O,BB}$ (van Velzen et al. 2020). As a result, the photosphere radius shrinks as $\dot{M}_{acc}$ decreases, with a faster evolution at smaller inclinations.

The ratio between UV/optical luminosity ($L_{O,BB}$) and X-ray luminosity ($L_{X,0.3-2\,keV}$) also decreases as the accretion level drops and the amount of obscuring material is reduced. The fastest $L_{O,BB}/L_{X,0.3-2\,keV}$ evolution is observed at intermediate inclinations, and especially if the TDE has a high accretion rate at peak. In such cases, we expect to see strong X-ray rebrightening of initially optically strong TDEs, as found in

ASASSN-15oi (Gezari et al. 2017). The X-ray luminosity reaches the same level as the UV/optical luminosity at $t \gtrsim 100$ days after peak, and possibly even later if the disk formation or viscous timescale is long. At very small inclinations, the event is always X-ray strong. At very large inclinations, the event should stay optically strong for a long period, although it is theoretically predicted that the disk should eventually become geometrically thin and emit mostly in X-rays/UV when the accretion level drops to around Eddington (Shakura & Sunyaev 1973).

While our model can qualitatively explain the evolution of most optical and X-ray TDEs, it cannot fully explain the evolution of ASASSN-14li, which produces almost equally bright in X-ray and UV/optical bands at peak and has $L_O/L_X \sim 1$ throughout the first year (Holoien et al. 2016). The unique behavior of ASASSN-14li could be related to the event happening in a host galaxy recently experiencing merger and AGN activities (Prieto et al. 2016). Another possible explanation is that ASASSN-14li could be observed from a low inclination that gives a slower L_O/L_X evolution, but we are currently missing some UV/optical emissions observed at low inclinations owing to our 1D reprocessing setup, which is explained more in Section 4.

In addition, we can compare the mass of the gas used for post-processing in the three simulations to the accumulated mass of the fallen-back debris at the particular epochs corresponding to those accretion rates. Using the fallback rate from Evans & Kochanek (1989) and the black hole and stellar parameters as above, the total debris mass that has fallen back between the peak and 45.9/102.4/174 days after the peak is $0.11/0.18/0.23\ M_\odot$, respectively, which is much larger than the mass of the gas needed for reprocessing ($0.012/0.024/0.072\ M_\odot$). It is worth mentioning that the effective mass used for the 1D post-processing can largely deviate from the true envelope mass owing to the highly asymmetric structure and mass distribution of the 3D disk. As an example, the effective 1D envelope masses for the $\dot{M}_{\rm acc} = 12\dot{M}_{\rm Edd}$ simulations in four inclination bins are listed in Table F1 to illustrate this effect.

4. Summary and Future Work

Inspired by the unified model for TDEs proposed in Dai et al. (2018), we carry out three additional 3D GRRMHD simulations of TDE super-Eddington accretion flow at different Eddington ratios and conduct radiative transfer calculations to obtain the emanating spectra. Based on the results, we further propose a dynamical unified model that can explain the diversity and evolution of TDE continuum emissions:

1. The viewing angle of the observer with respect to the orientation of the disk is the most important parameter in determining whether we observe either an X-ray or an optical bright TDE. At small inclinations, X-rays can escape from the funnel of the super-Eddington disk. At large inclinations, X-rays are mostly reprocessed into UV/optical radiation by the geometrically and optically thick wind and disk.

2. The blackbody radiation fits of the TDE super-Eddington disk spectra produce color temperature, blackbody luminosity, and photosphere radius distributions consistent with the observed ones. Most radiative energy escapes in the EUV range, and only a few to a few tens of percentage of radiative energy can be detected, which

provides a solution to the TDE missing energy problem. The deviation between the detected energy and total energy is more severe for optical TDEs than X-ray TDEs.

3. The observed diversity of the emission from different TDEs can be associated with the different Eddington ratios of their accretion rates, $\dot{M}_{\rm acc} = {\rm few} \times (1 - 10)\ \dot{M}_{\rm Edd}$, at the flare peak conditions. In general, higher accretion levels induce larger (fitted blackbody) luminosities and larger photosphere radii but do not significantly change the fitted effective temperatures.

4. The early-time evolution ($t \approx 100$ days after peak) of optical TDEs can be explained by this reprocessing model. As the luminosity drops by about 0.5–1 orders of magnitude, the fitted temperature slightly increases at small to intermediate inclinations or decreases at large inclinations.

5. The evolution of the optical-to-X-ray flux ratio also depends sensitively on the viewing angle. At large inclinations, the TDE stays UV/optically strong for a very long time. At intermediate inclinations, we expect to see the fastest X-ray rebrightening, and L_O/L_X reaches unity at a few hundred days. At small inclinations, the TDE is always X-ray strong. The exact evolution timescale also depends on the accretion rate at peak, which further depends on the black hole and stellar parameters.

Many TDEs also exhibit distinct spectroscopic properties. In the optical range, TDEs can be characterized by producing strong and broad H, or He, or Bowen fluorescence emission lines or being featureless (Leloudas et al. 2019; van Velzen et al. 2020; Charalampopoulos et al. 2022; Hammerstein et al. 2022). Their UV spectra can display broad absorption line (BAL) or broad emission line (BEL) features as also observed in some types of quasars (Hung et al. 2019). Some theoretical work has been done to understand TDE spectra. In particular, Parkinson et al. (2020, 2022) have modeled TDE UV/optical continuum and line spectra also based on a reprocessing model. They adopted a biconical 2D disk wind toy model, somewhat similar to ours, but they focused on the phases after peak when the accretion rate and wind mass rate both drop below the Eddington level. They injected a broadened blackbody spectrum of a thin disk and showed that the reprocessing can produce continuum fitting the observed optical TDEs as well as BAL or BEL features depending on whether the observer's line of sight intersects the wind. Compared to our model, the level of reprocessing is much less in theirs owing to the low wind density, and as a result their X-rays are not completely absorbed from any inclination. In addition, in the current work we have not studied the TDE line proprieties, since our current Sedona simulations do not have frequency grids fine enough to fully capture the bound–bound transitions. In a future work, we plan to address this issue and conduct TDE spectroscopic modelings.

Furthermore, while our GRRMHD simulations are conducted in 3D, we have done post-processing using a 1D setting, i.e., we use the gas profile inside a particular inclination bin and assume that it is spherically symmetric. This means that when viewing a TDE at low inclinations, due to the geometric effects, we only include the emissions leaked out from the funnel regions but miss those from the wind/outer disk. Therefore, we could have underestimated the optical emissions observed from

low inclinations. In addition, as shown by Parkinson et al. (2020, 2022), implementing 2D or 3D radiative transfer calculations can allow one to follow photons along more realistic paths, which induce effects such as the reduction of photon trapping in the wind. We will also work toward including 2D/3D radiative transfer calculations in our post-processing simulation.

In this work we have varied the accretion rate while keeping the same black hole mass and spin parameters. If adopting the thin-disk model, one expects that TDEs from more massive black holes should produce a higher L_O/L_X owing to the combined effects on disk temperatures from larger black hole mass and lower fallback/accretion rate. However, our calculation shows that in the super-Eddington regime more X-rays can leak out as the accretion rate drops. Therefore, the dependence between TDE emission and black hole mass might be subtle owing to these two opposite effects. The black hole spin is expected to be important for the funnel structure, jet launching, and therefore the production of non-thermal X-ray emissions. Future work studying how black hole parameters affect TDE emissions will enhance our understanding of not only TDEs but also other super-Eddington systems such as ultraluminous X-ray sources.

Last but not least, a series of reprocessing models have been raised to explain TDE optical emissions, most of which employ a spherically symmetric envelope for the calculations (e.g., Metzger & Stone 2016; Roth et al. 2016; Matsumoto & Piran 2021). While these 1D models offer insights for the radiative transfer physics and our post-processing calculations are also conducted under a 1D setting, it is important to emphasize that the real reprocessing gaseous envelope likely has asymmetric structure and mass distributions (as constrained using polarimetry by Leloudas et al. 2022), so 1D calculations can overestimate the mass needed for reprocessing. Using disk structures from 3D novel simulations, we have demonstrated that the stellar debris mass fallen back at early time is sufficient to reprocess most X-rays into UV/optical emissions when the observer is viewing from relatively large inclinations.

Appendix A
Properties of Simulated Disks

A few more time-averaged quantities of the three simulated disks are listed in Table A1. Φ_H is the normalized magnetic flux at horizon Φ_H (Tchekhovskoy et al. 2011), with $\Phi_H \gtrsim 30 - 40$ being the condition for MADs. The net accretion efficiency η_H evaluates how much rest-mass energy going into the black hole is converted to outgoing energy near the event horizon. L_{jet} is the total power of the relativistic jet at $r = 5500 r_g$, most of which is in the form of electromagnetic energy. $\Gamma_{jet,max}$ is the maximum Lorentz factor of the jet. L_K is the thermal+kinetic luminosity of the wind calculated at $r \sim 5500 r_g$. α_{eff} is the effective α-parameter of the disk as defined in McKinney et al. (2012). R_{eq} indicates the radius within which the disk inflow equilibrium has been established. In our simulations, the winds are launched mostly from the inner disk regions and have traveled beyond the photospheres at most inclination angles.

Table A1
More Disk Quantities

Model	$\dot{M}_{acc}(\dot{M}_{Edd})$	Φ_H	η_H (%)	$L_{jet}(L_{Edd})$	$\Gamma_{jet,max}$	$L_K(L_{Edd})$	α_{eff}	$R_{eq}(R_g)$
M6a08-1	7	34.5	35.5	1.1	2.27	0.5	2.7	340
M6a08-2	12	39	40.1	2.3	2.39	1.0	3.3	320
M6a08-3	24	55	69.3	9.7	2.66	4.8	2.3	230

Appendix B
Radiative Transfer Physics

In our radiative transfer calculations, the X-rays, injected from the inner disk, are reprocessed mainly owing to three mechanisms:

1. "Adiabatic expansion": The accumulation of multiple scatterings of photons in a diverging, fast-moving, optically thick wind can increase the photon wavelength owing to Doppler shift. In the limit that the photons remain fully trapped, the change in the radiation energy density can be computed based on the thermodynamics of adiabatic expansion. For the radiative transfer calculations in this paper, the fully adiabatic limit does not apply, but the result is still that photon energies are downgraded as they traverse the wind. The amount of photon energy change depends on the velocity divergence of the wind and the number of scatterings photons undergo before they escape.

2. Absorption and reemission: The absorption of X-rays in the accretion flow is dominated by bound–free interactions. Each bound–free absorption event acts as a heating source for the free electrons. Meanwhile, free electrons can recombine to produce fluorescence lines, which is a cooling mechanism for the free electrons. The amount of bound–free absorption depends on the number of bound electrons available to be ionized at a given location.

3. Compton scattering: Electron recoil causes scattering events to be noncoherent in the fluid rest frame, heating the electrons and downgrading the photon energies. Meanwhile, thermal motion of electrons can transfer energy from the electrons to the photons when the electron temperature is sufficiently high. With typical gas temperature between 10^6 and 10^4 K in our accretion flow, X-ray photons are expected to overall lose energy and optical photons will gain energy owing to Compton scattering. We note in the latter case (direct Compton scattering) that the induced electron temperature change is not included in this version of SEDONA. One can estimate how important Compton scattering

is by calculating the Compton y parameter, which is the average energy change per scattering times the number of scatterings. If inverse Compton scattering dominates, we have $y_{IC} = kT_{eff}/(m_e c^2) \times \max(\tau_{es}, \tau_{es}^2)$, and if Compton scattering dominates, we have $y_C = h\nu/(m_e c^2) \times \max(\tau_{es}, \tau_{es}^2)$. Here k is the Stefan–Boltzmann constant, m_e is the electron mass, T_e is the electron temperature, and T_{eff} is the optical-depth-averaged gas temperature $T_{eff} = \int T\kappa_{es}\rho dr/\tau_{es}$, where κ_{es} is the electron-scattering opacity and τ_{es} is the total electron-scattering optical depth.

In Figure B1, we highlight the importance of the three reprocessing mechanisms in gas with different physical conditions. We choose a low-inclination case ($i = 30°$) where the wind velocity is very high and a high-inclination case ($i = 70°$) where the wind optical depth is very large. We plot the spectra and the corresponding wavelength-dependent optical depth (the sum of scattering and all absorption opacities). For the low-inclination case, we see that only the photoionization cross sections of O VII and O VIII contribute a small amount to the overall optical depth, since the gas is almost totally ionized and we are dominated by electron scattering. Therefore, absorption is not effective for reprocessing for this case, and neither is inverse Comptonization since $y_{IC} = 0.002$ owing to the dilute wind. What reddens the escaped spectrum compared to the injected spectrum is mostly the adiabatic expansion with a small contribution from Compton scattering of X-ray photons (e.g., $y_C = 0.2$ for $\lambda = 10$ Å). For the high-inclination case, gas is much denser and cannot be fully ionized by the injected radiation. The optical depth is very large owing to the photoionization of different oxygen species existing throughout the wind, as well as some helium. Therefore, the spectral flux is largely suppressed by O and He absorption. The large absorption opacities for X-ray photons lessen the importance of Compton scattering. Although we have, e.g., $y_C = 459$ for $\lambda = 10$ Å, X-rays would still be all reprocessed even if Compton scattering was not included, and the overall optical continuum level would remain similar. Therefore, the reprocessing in the high-density case is mostly set by the bound–free interactions.
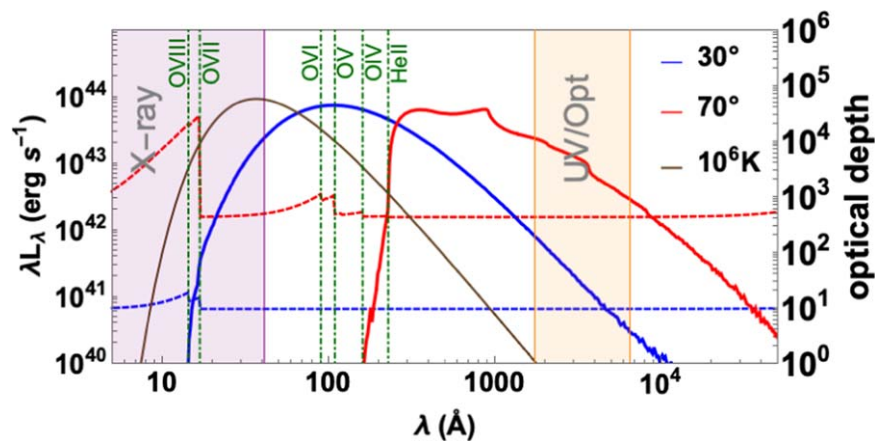
Figure B 1. The optical depth as a function of the wavelength (dashed curve) overlaid with the escaped spectra (solid curve) at two different inclinations $i = 30°$ and $i = 70°$ for the simulation with $\dot{M}_{acc} = 12\ \dot{M}_{Edd}$ and $L_{bol} = L_{Edd}$. The injected Planck spectrum at $T = 10^6$ K (brown thin curve) is also plotted to show the level of reprocessing. The photoionization edges have been marked with the green vertical lines and labeled.

Appendix C
Simulated Spectra at Higher Luminosity

Spectra are also plotted for the other luminosity setting with $L_{bol} = 10\% \times \dot{M}_{acc} c^2$ and shown in Figure C1.
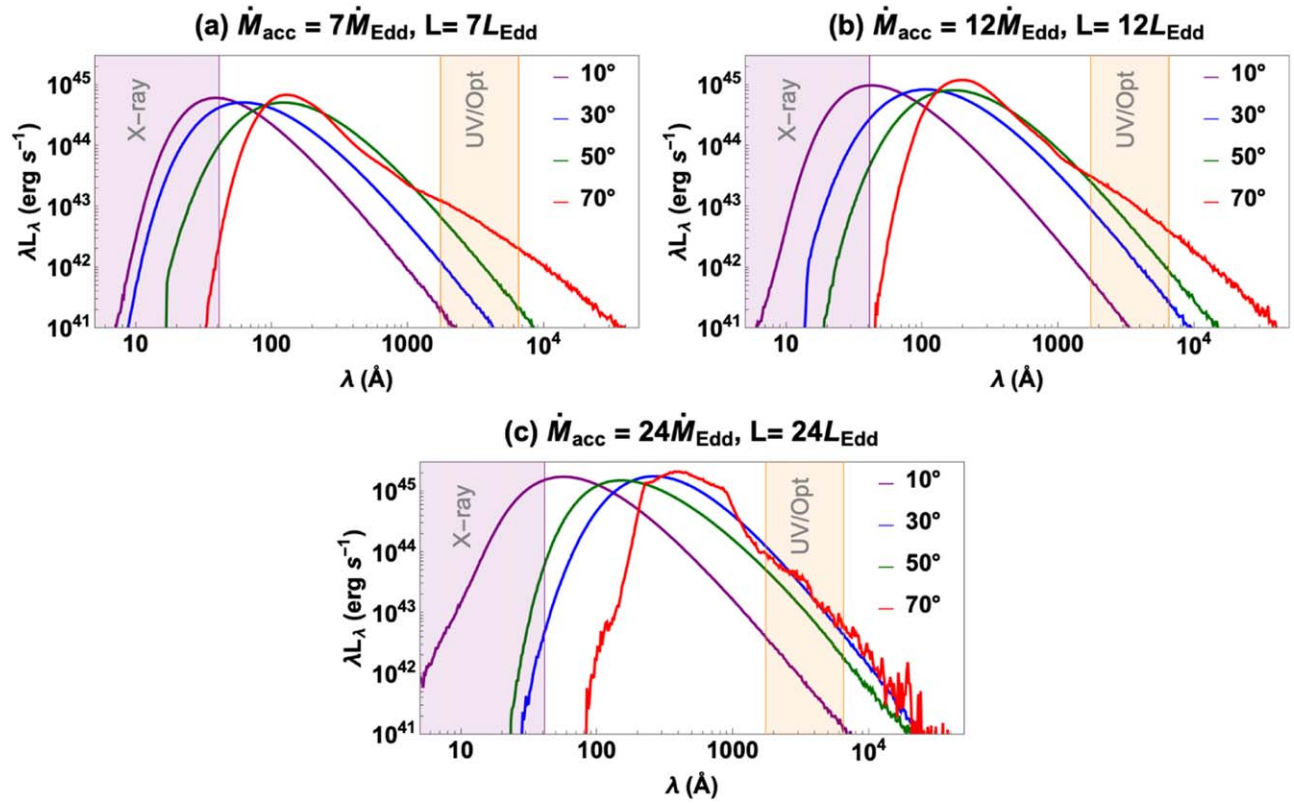

Figure C1. The simulated escaping spectra of the accretion disk at different accretion rates and inclinations, similar to Figures 2(a)–(c), except that the bolometric luminosity of the spectra $L_{bol} = 10\% \times \dot{M}_{acc} c^2$.

Appendix D
List of Observed TDEs Reported in the Literature

For plotting Figures 3(a)–(c) we use 16 optically selected TDEs and 7 X-ray-selected TDEs. For completeness we list their names and relevant parameters as reported from previous literature in Tables D1 and D2.

Table D1
Names and Parameters of Optical TDEs

Name	$\log M_{\mathrm{BH}}$ ($M_\odot$)	$\log L_{\mathrm{BB}}$ (erg s^{-1})	$\log T_{\mathrm{BB}}$ (K)	$\log R_{\mathrm{BB}}$ (R_g)
ASASSN-14ae	5.42	43.87	4.29	4.34
ASASSN-14li	6.31	43.66	4.52	2.88
ASASSN-15lh	8.47	45.34	4.30	2.00
ASASSN-15oi	5.71	44.45	4.60	3.72
AT2018dyb/ASASSN-18pg	6.67	44.08	4.40	2.97
AT2018hyz/ASASSN-18zj	5.68	44.10	4.25	4.27
GALEXD1-9	6.51	43.48	4.59	2.45
GALEXD23H-1	6.39	43.95	4.70	2.59
GALEXD3-13	7.36	43.98	4.66	1.71
iPTF-15af	6.88	44.10	4.85	1.87
iPTF-16axa	6.34	43.82	4.46	3.05
PS1-10jh	5.85	44.47	4.59	3.61
PTF-09axc	5.68	43.46	4.08	4.29
PTF-09djl	5.82	44.42	4.41	3.97
PTF-09ge	6.34	44.04	4.08	3.92
SDSS-TDE1	7.24	43.64	4.42	2.14

Table D2
Names and Parameters of X-ray TDEs

Name	$\log M_{\mathrm{BH}}$ ($M_\odot$)	$\log L_{\mathrm{BB}}$ (erg s^{-1})	$\log T_{\mathrm{BB}}$ (K)	$\log R_{\mathrm{BB}}$ (R_g)
SDSS J1323+48	6.15	44.30	5.91	0.80
SDSS J1201+30	7.18	45.00	6.06	−0.29
RX J1624+75	7.68	43.38	6.05	−1.57
RX J1420+53	7.33	43.38	5.67	0.03
RBS 1032	5.25	41.70	6.11	−0.13
3XMM J1521+07	5.61	43.51	6.30	−0.02
3XMM J1500+01	5.64	43.08	6.06	0.29

Appendix E
Modeled TDE Parameters

The values of the modeled observable as in Figures 3(d)–(i) are listed in Table E1. The modeled bolometric correction, which is defined as $(L_{O,BB} + (L_{X,BB})/L_{bol}$, is plotted in Figure E1.

Table E1
Modeled TDE Observables

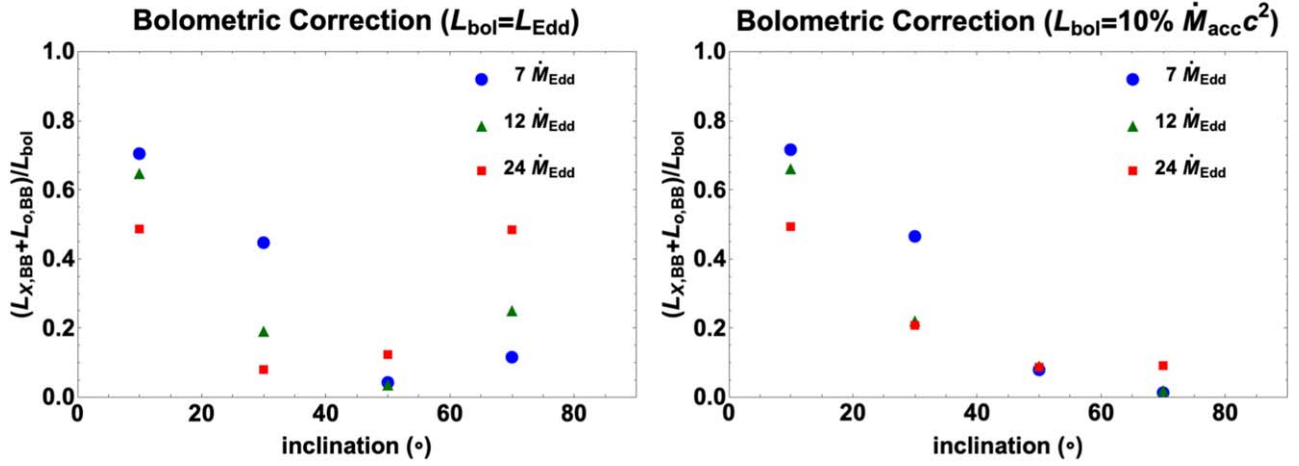| $\dot{M}_{acc}$ ($\dot{M}_{Edd}$)	L_{bol} (L_{Edd})	Inc. (deg)	log $L_{O,BB}$ (erg s^{-1})	$L_{O,BB}/L_{bol}$	log $T_{O,BB}$ (K)	log $R_{O,BB}$ (cm)	log $L_{X,BB}$ (erg s^{-1})	$L_{X,BB}/L_{bol}$	log $T_{X,BB}$ (K)	log $R_{X,BB}$ (cm)
7	1	10	40.650	0.000	4.47	12.71	43.952	0.710	5.99	11.38
		30	42.212	0.013	4.89	12.64	43.742	0.438	5.91	11.45
		50	42.480	0.024	4.67	13.48	42.475	0.024	5.72	11.85
		70	43.179	0.120	4.30	14.55	38.879	0.000	5.25	13.11
	7	10	42.861	0.008	5.13	12.50	44.799	0.713	5.99	11.80
		30	43.434	0.031	5.04	12.95	44.587	0.438	5.91	11.87
		50	43.691	0.056	4.85	13.72	43.407	0.029	5.74	12.29
		70	43.175	0.017	4.30	14.55	41.422	0.000	5.35	13.55
12	1	10	40.989	0.001	4.55	12.73	43.914	0.651	5.98	11.38
		30	42.503	0.025	4.74	13.09	43.334	0.171	5.78	11.61
		50	42.684	0.038	4.54	13.84	41.451	0.002	5.57	12.05
		70	43.508	0.255	4.38	14.57	⋯	⋯	⋯	⋯
	12	10	43.364	0.015	5.13	12.75	44.994	0.652	5.99	11.91
		30	43.921	0.055	4.89	13.50	44.413	0.171	5.78	12.15
		50	44.130	0.089	4.78	14.08	42.973	0.006	5.65	12.40
		70	43.558	0.024	4.34	14.66	⋯	⋯	⋯	⋯
24	1	10	41.407	0.002	4.44	13.15	43.786	0.483	5.98	11.30
		30	42.994	0.078	4.53	13.75	41.452	0.002	5.40	12.17
		50	43.193	0.123	4.48	14.20	⋯	⋯	⋯	⋯
		70	43.784	0.482	4.41	14.64	⋯	⋯	⋯	⋯
	24	10	43.427	0.009	4.83	13.37	45.167	0.485	5.99	11.97
		30	44.790	0.204	4.77	14.18	42.977	0.003	5.43	12.80
		50	44.401	0.083	4.76	14.26	43.026	0.004	5.50	13.22
		70	44.444	0.092	4.67	14.46	⋯	⋯	⋯	⋯

Figure E1. The modeled bolometric correction $(L_{O,BB} + (L_{X,BB})/L_{bol}$ for two escaped luminosity settings. One can see that the luminosity inferred from the observations based on the assumption of blackbody radiation usually misses a large portion of the bolometric luminosity, and this problem is more severe for optical TDEs.

Appendix F
Characteristic Timescales

There are various physical timescales relevant for TDEs: debris mass fallback timescale, disk formation/circularization timescale, disk viscous timescale, and photon transport timescale. The longest timescale of all governs the temporal evolution of TDE emissions.

The photon transport time through an optically thick medium is the shorter one between the diffusion timescale and advection timescale. The photon diffusion timescale is calculated as $t_{diff} = \tau_{es} R_{es}/c$, where R_{es} is the size of the electron-scattering photosphere along a particular inclination and τ_{es} is the electron-scattering optical depth integrated radially from $r = 0$ to $r = R_{es}$. The advection timescale is calculated as $t_{adv} \approx R_{es}/v_r$, since the photons trapped by the optically thick gas have a similar speed to the gas. Here the gas radial velocity v_r is averaged over the radial path within R_{es} and weighted by gas density. The values of these timescales in the $\dot{M}_{acc} = 12\dot{M}_{Edd}$ accretion flow are given in Table F1. One can see that, for the inclinations considered in this work, photons are preferably advected out by the optically thick wind. The photon transport time varies from ~ 0.1 to a few days depending on the inclination.

The disk viscous timescale can be analytically calculated by $t_{visc} = t_{dyn} \alpha^{-1} (H/R)^{-2}$, where t_{dyn} is the orbital timescale of the disk, α is a free parameter between 0 and approximately 1, and H/R is the disk thickness (Shakura & Sunyaev 1973). For our disk parameters, we have $t_{visc} \approx 5.44$ days $(R_{disk}/8500r_g)(M_{BH}/10^6 M_\odot)(\alpha/1)^{-1}((H/R)/0.3)^{-2}$. The viscous time is therefore only a few days. We caution the readers that our simulated disks are MADs, which typically have effective $\alpha \gtrsim 1$. The viscous time is potentially longer if the disks do not have such large magnetic fluxes.

The disk formation/circularization timescale induces uncertainty into the evolution of TDEs. Recent simulations show that a large fraction of the debris materials can form a disk within a dynamical timescale, but the disk still possesses some moderate eccentricity (Bonnerot et al. 2021). As the topic is out of the scope of this paper, we assume here that the disk forms quickly for the calculation of the emission evolution.

Stellar debris typically falls back on timescales of t_{mb}, which is the orbital time of the most bound debris (Evans &

Table F1
Photon Diffusion and Advection Timescales for the Simulated Disk at $\dot{M}_{acc} = 12\dot{M}_{Edd}$

Quantities \ Inclination (deg)	10	30	50	70
R_{es} (R_g)	896	1278	5425	8377
τ_{es}	7.0	74.0	137.2	710.2
v_r (c)	0.50	0.35	0.13	0.013
t_{adv} (days)	0.07	0.13	1.06	13.6
t_{diff} (days)	0.35	5.4	42.2	337.4
1D envelope mass ($M_\odot$)	0.004	0.004	0.02	0.4

Table F2
Time Elapsed since Peak Corresponding to the Three Simulated TDE Disks, Assuming $M_{BH} = 10^6 M_\odot$ and Various Different $m_\star$

Quantities \ $m_\star$ ($M_\odot$)	0.2	0.5	1	1.5
$\dot{M}_{fb,peak}$ ($\dot{M}_{Edd}$)	36.7	76.4	133.0	211.6
$t_{pp}(\dot{M}_{fb} = (24+14) \dot{M}_{Edd})$ (days)	NA	18.6	45.9	69.7
$t_{pp}(\dot{M}_{fb} = (12+4.5) \dot{M}_{Edd})$ (days)	18.3	53.8	102.4	140.0
$t_{pp}(\dot{M}_{fb} = (7+1.4) \dot{M}_{Edd})$ (days)	42.3	98.5	174.0	229.2

Kochanek 1989; Guillochon & Ramirez-Ruiz 2013; Rossi et al. 2021):

$$t_{mb} \approx 41 \text{ days} \left(\frac{M_{BH}}{10^6 M_\odot}\right)^{1/2} \left(\frac{m_\star}{M_\odot}\right)^{-1} \left(\frac{r_\star}{R_\odot}\right)^{3/2}. \quad (F1)$$

For our case with $M_{BH} = 10^6 M_\odot$, t_{mb} varies between 25 and 41 days for $m_\star = 0.1 - 10 M_\odot$.

Lastly, assuming that the fallback timescale governs the evolution of TDEs, we calculate the time corresponding to each simulated disk with a further assumption that the fallback rate $\dot{M}_{fb}$ equals the instantaneous accretion rate $\dot{M}_{acc}$ plus the wind mass rate $\dot{M}_w$. Here we focus on the post-peak evolution. By

setting that the fallback rate peaks at t_{mb}, the post-peak time t_{pp} associated with a particular $\dot{M}_{fb}$ can be calculated with

$$\dot{M}_{fb} \approx 133 \left(\frac{M_{BH}}{10^6\,M_\odot}\right)^{-3/2} \left(\frac{m_\star}{M_\odot}\right)^2 \left(\frac{r_\star}{R_\odot}\right)^{-3/2} \left(\frac{t}{t_{mb}}\right)^{-5/3} \dot{M}_{Edd}.$$

(F2)

With the wind mass rate given in Table 1, the three simulated disks correspond to $\dot{M}_{fb} = \dot{M}_{acc} + \dot{M}_w = (7 + 1.4, 12 + 4.5, 24 + 14)\,\dot{M}_{Edd}$. The post-peak time obtained with $M_{BH} = 10^6\,M_\odot$ and a few different $m_\star$ are shown in Table F2.

ORCID iDs

Lars L. Thomsen ⬤ https://orcid.org/0000-0003-4256-7059
Tom M. Kwan ⬤ https://orcid.org/0000-0003-0509-2541
Lixin Dai ⬤ https://orcid.org/0000-0002-9589-5235
Samantha C. Wu ⬤ https://orcid.org/0000-0003-2872-5153
Nathaniel Roth ⬤ https://orcid.org/0000-0002-6485-2259
Enrico Ramirez-Ruiz ⬤ https://orcid.org/0000-0003-2558-3102

References

Andalman, Z. L., Liska, M. T. P., Tchekhovskoy, A., Coughlin, E. R., & Stone, N. 2022, MNRAS, 510, 1627
Auchettl, K., Guillochon, J., & Ramirez-Ruiz, E. 2017, ApJ, 838, 149
Balbus, S. A., & Hawley, J. F. 1998, RvMP, 70, 1
Blandford, R. D., & Znajek, R. L. 1977, MNRAS, 179, 433
Bloom, J. S., Giannios, D., Metzger, B. D., et al. 2011, Sci, 333, 203
Bonnerot, C., Lu, W., & Hopkins, P. F. 2021, MNRAS, 504, 4885
Burrows, D. N., Kennea, J. A., Ghisellini, G., et al. 2011, Natur, 476, 421
Cenko, S. B., Krimm, H. A., Horesh, A., et al. 2012, ApJ, 753, 77
Charalampopoulos, P., Leloudas, G., Malesani, D. B., et al. 2022, A&A, 659, A34
Coughlin, E. R., & Begelman, M. C. 2014, ApJ, 781, 82
Curd, B., & Narayan, R. 2019, MNRAS, 483, 565
Dai, J. L., Lodato, G., & Cheng, R. 2021, SSRv, 217, 12
Dai, L., McKinney, J. C., & Miller, M. C. 2015, ApJL, 812, L39
Dai, L., McKinney, J. C., Roth, N., Ramirez-Ruiz, E., & Miller, M. C. 2018, ApJL, 859, L20
De Colle, F., Guillochon, J., Naiman, J., & Ramirez-Ruiz, E. 2012, ApJ, 760, 103
Evans, C. R., & Kochanek, C. S. 1989, ApJL, 346, L13
French, K. D., Wevers, T., Law-Smith, J., Graur, O., & Zabludoff, A. I. 2020, SSRv, 216, 32
Gezari, S. 2021, ARA&A, 59, 21
Gezari, S., Cenko, S. B., & Arcavi, I. 2017, ApJL, 851, L47
Guillochon, J., Manukian, H., & Ramirez-Ruiz, E. 2014, ApJ, 783, 23
Guillochon, J., & Ramirez-Ruiz, E. 2013, ApJ, 767, 25
Hammerstein, E., van Velzen, S., Gezari, S., et al. 2022, arXiv:2203.01461

Hayasaki, K., & Jonker, P. G. 2021, ApJ, 921, 20
Hinkle, J. T., Holoien, T. W. S., Auchettl, K., et al. 2021, MNRAS, 500, 1673
Holoien, T. W. S., Brown, J. S., Auchettl, K., et al. 2018, MNRAS, 480, 5689
Holoien, T. W.-S., Kochanek, C. S., Prieto, J. L., et al. 2016, MNRAS, 455, 2918
Hung, T., Cenko, S. B., Roth, N., et al. 2019, ApJ, 879, 119
Jiang, Y.-F., Stone, J. M., & Davis, S. W. 2014, ApJ, 796, 106
Jiang, Y.-F., Stone, J. M., & Davis, S. W. 2019, ApJ, 880, 67
Kasen, D., Thomas, R. C., & Nugent, P. 2006, ApJ, 651, 366
Law-Smith, J. A. P., Coulter, D. A., Guillochon, J., Mockler, B., & Ramirez-Ruiz, E. 2020, ApJ, 905, 141
Leloudas, G., Bulla, M., Cikota, A., et al. 2022, arXiv:2207.06855
Leloudas, G., Dai, L., Arcavi, I., et al. 2019, ApJ, 887, 218
Liu, X.-L., Dou, L.-M., Chen, J.-H., & Shen, R.-F. 2022, ApJ, 925, 67
Lodato, G., & Rossi, E. M. 2011, MNRAS, 410, 359
Loeb, A., & Ulmer, A. 1997, ApJ, 489, 573
Lu, W., & Kumar, P. 2018, ApJ, 865, 128
Matsumoto, T., & Piran, T. 2021, MNRAS, 502, 3385
McKinney, J. C., Dai, L., & Avara, M. J. 2015, MNRAS, 454, L6
McKinney, J. C., Tchekhovskoy, A., & Blandford, R. D. 2012, MNRAS, 423, 3083
McKinney, J. C., Tchekhovskoy, A., Sadowski, A., & Narayan, R. 2014, MNRAS, 441, 3177
Metzger, B. D., & Stone, N. C. 2016, MNRAS, 461, 948
Mockler, B., Guillochon, J., & Ramirez-Ruiz, E. 2019, ApJ, 872, 151
Mockler, B., & Ramirez-Ruiz, E. 2021, ApJ, 906, 101
Narayan, R., Igumenshchev, I. V., & Abramowicz, M. A. 2003, PASJ, 55, L69
Novikov, I. D., & Thorne, K. S. 1973, in Black Holes (Les Astres Occlus), ed. C. Dewitt & B. S Dewitt (New York: Gordon and Breach), 343
Parkinson, E. J., Knigge, C., Long, K. S., et al. 2020, MNRAS, 494, 4914
Parkinson, E. J., Knigge, C., Matthews, J. H., et al. 2022, MNRAS, 510, 5426
Pfister, H., Volonteri, M., Dai, J. L., & Colpi, M. 2020, MNRAS, 497, 2276
Piran, T., Svirski, G., Krolik, J., Cheng, R. M., & Shiokawa, H. 2015, ApJ, 806, 164
Prieto, J. L., Krühler, T., Anderson, J. P., et al. 2016, ApJL, 830, L32
Ramirez-Ruiz, E., & Rosswog, S. 2009, ApJL, 697, L77
Rees, M. J. 1988, Natur, 333, 523
Rossi, E. M., Stone, N. C., Law-Smith, J. A. P., et al. 2021, SSRv, 217, 40
Roth, N., & Kasen, D. 2018, ApJ, 855, 54
Roth, N., Kasen, D., Guillochon, J., & Ramirez-Ruiz, E. 2016, ApJ, 827, 3
Roth, N., Rossi, E. M., Krolik, J., et al. 2020, SSRv, 216, 114
Sądowski, A, & Narayan, R 2016, MNRAS, 456, 3929
Saxton, R., Komossa, S., Auchettl, K., & Jonker, P. G. 2021, SSRv, 217, 18
Sazonov, S., Gilfanov, M., Medvedev, P., et al. 2021, MNRAS, 508, 3820
Shakura, N. I., & Sunyaev, R. A. 1973, A&A, 24, 337
Stone, N. C., & Metzger, B. D. 2016, MNRAS, 455, 859
Stone, N. C., Vasiliev, E., Kesden, M., et al. 2020, SSRv, 216, 35
Strubbe, L. E., & Quataert, E. 2009, MNRAS, 400, 2070
Tchekhovskoy, A., Narayan, R., & McKinney, J. C. 2011, MNRAS, 418, L79
Ulmer, A. 1999, ApJ, 514, 180
van Velzen, S., Holoien, T. W. S., Onori, F., Hung, T., & Arcavi, I. 2020, SSRv, 216, 124
van Velzen, S., Stone, N. C., Metzger, B. D., et al. 2019, ApJ, 878, 82
Wevers, T., Pasham, D. R., van Velzen, S., et al. 2019, MNRAS, 488, 4816
Wong, T. H. T., Pfister, H., & Dai, L. 2022, ApJL, 927, L19
Yao, Y., Lu, W., Guolo, M., et al. 2022, ApJ, 937, 8